# Additive Manufacturing of Flexible Strain Sensors Based on Smart Composites for Structural Health Monitoring with High Accuracy and Fidelity

*Sheraz Ahmed, Mahdi Bodaghi,\* Saad Nauman,\* and Zaffar Muhammad Khan*

This research introduces a novel flexible spherical carbon nanoparticle-based polyurethane conductive ink, which is employed to fabricate strain sensors by a lab-developed direct ink writing/3D printing system. Rheological tests are performed, and sensors are pasted on glass fiber-reinforced plastic specimens to study strain gauge behaviors under quasistatic loading. The gauge factor in tensile loading is found to be layer width dependent as decreasing the strain gauge's layer width increases the sensitivity of the strain sensor. A maximum gauge factor of 34 is achieved using a layer width of 0.2 mm, 17 times greater than commercially available metal foil strain gauges. The four-point bend tests are performed under tension/compression to assess the sensor's strain-sensing and damage-monitoring ability. Fractographic analysis is coupled with strain monitoring using the developed sensor, which confirms that the failure progresses from intralaminar failure modes such as ply splitting in tension. At the same time, delamination leads to kink band formation under compression and the eventual failure of load-bearing fibers. The developed sensor exhibits repeatable performance with low hysteresis and integrated nonlinearity errors for up to 1000 cycles. The developed sensors could be effectively employed for online in situ structural health monitoring of aerospace structures under static and dynamic loading.

## 1. Introduction

Owing to the sophistication of aircraft structures, detailed disassembly and reassembly is required for inspection. Due to the complexity of its structure, certain critical sections of the aircraft are not readily accessible for inspection.[1,2] Even though maintenance in aerospace structures needs excessive amount of man power and man hours, some of the hidden subsurface cracks may still remain undetected.[3–6] In addition to the direct cost of inspection and repair (materials, labor, etc.), the indirect costs related to the withdrawal of the aircraft from operation have a greater economic effect on the user.[7] Many conventional nondestructive testing (NDT) methodologies[8] such as X-ray tomography,[9] eddy current analysis,[10] ultrasound monitoring,[11] etc. are used for noninvasive inspection of aircrafts.[12]

Structural health monitoring (SHM) is fast emerging as an alternative paradigm. Unlike traditional NDT systems, a distinguishing feature of SHM is that the system's sensors and actuators are permanently attached to the device, gathering whole field data almost continuously for the entire service life of the structure, without operator interference.[12–16] NDT is used to detect discontinuities in solids that are recognized as damage, either on the surface or inside.[17] On the other hand, SHM senses local changes in the structure, either in the properties of the material or its functionality.[12,16,18] These changes are detected by comparing the structure's response to a stimulus with that of the pristine structure's response.[19,20] In terms of its implementation and design, SHM is a multidisciplinary domain that employs different sensors, including strain gauges,[21,22] acoustic probes,[23] interferometry, and fiber Bragg grating (FBG) sensors.[24] Aerospace structures use strain gauges for timely damage detection, monitoring crack propagation and averting catastrophic failures. By incorporating SHM system in an aircraft structure,

S. Ahmed, S. Nauman
Department of Materials Science & Engineering
Institute of Space Technology
Islamabad 44000, Pakistan
E-mail: saad.nauman@ist.edu.pk

The ORCID identification number(s) for the author(s) of this article can be found under https://doi.org/10.1002/adem.202300763.

M. Bodaghi
Department of Engineering
School of Science and Technology
Nottingham Trent University
Nottingham NG11 8NS, UK
E-mail: mahdi.bodaghi@ntu.ac.uk

Z. Muhammad Khan
Department of Aeronautics & Astronautics
Institute of Space Technology
Islamabad 44000, Pakistan

Z. Muhammad Khan
Department of Mechanical Engineering
University of Technology
Nowshera, Pakistan

designer would not have to overbuild the wing structure to stiffen it which adds weight to the aircraft.[25] With a reliable and sensitive sensor, designer would have the freedom to create new damage tolerant designs for hypersonic aircraft and spacecraft.

Flexible polymeric sensors offer significant advantages as compared to metal foil strain sensors, such as high sensitivity, high strain-measuring capability, elevated elongation at break, and ease of application on complex structures.[26–29] Several polymeric composite materials are used to develop strain sensors, such as thermoplastic polyurethane (TPU), polystyrene (PS), thermoplastic polyethylene (TPE), polydimethylsiloxane (PDMS), silicon, rubbers, etc. as matrix material.[30–32] At the same time, graphene, carbon nanotubes, and silver nanoparticles have been widely used as conductive fillers to develop conductive percolation networks.[33–46] Various researchers have reported strain sensors fabricated through fused deposition modeling (FDM)/3D printing, electrospinning technologies, etc.[47–52]
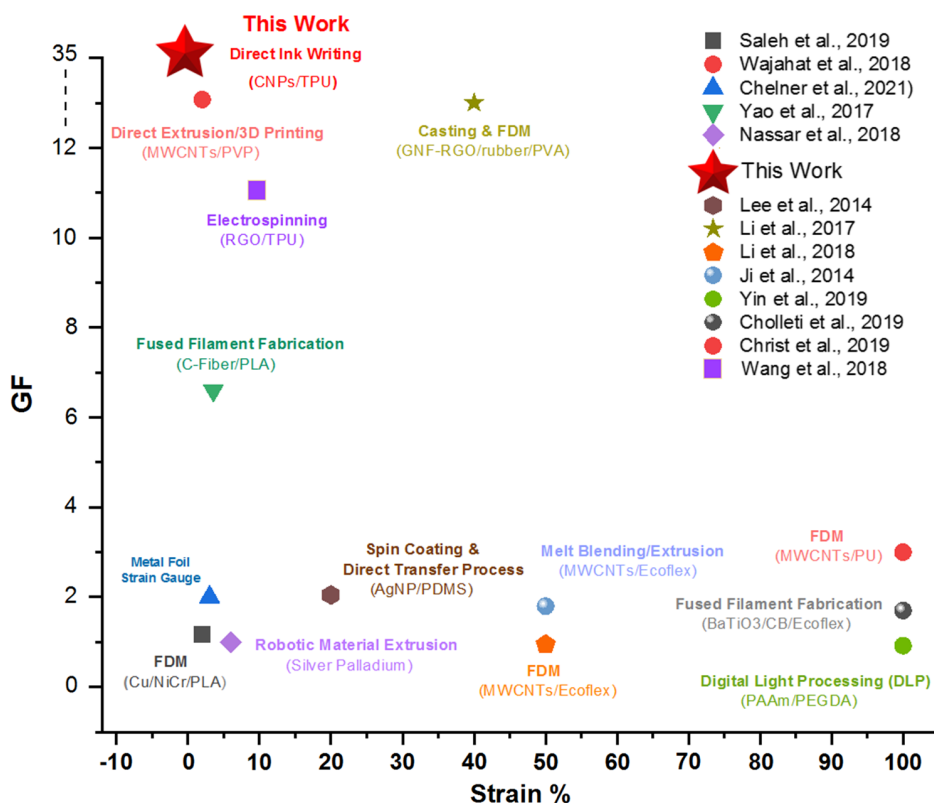


**Figure 1.** A comparison between already developed sensors with the current work in terms of GF.
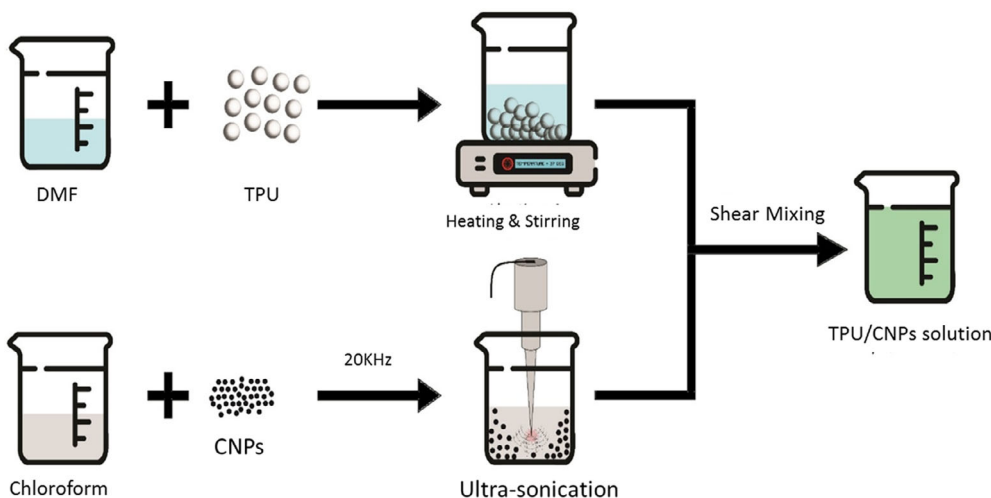


**Figure 2.** Schematic showing CNPs/DMF dispersion and TPU/DMF CPC solution.

**ADVANCED
SCIENCE NEWS**

www.advancedsciencenews.com

**ADVANCED
ENGINEERING
MATERIALS**

www.aem-journal.com

Some research has been devoted to conductive fillers such as graphene, carbon nanotubes, silver, and graphite.[53–57] However, to the best of authors' knowledge, limited work has been dedicated to carbon-based spherical nanoparticles and further research is needed to study the effect of real-time monitoring ability by incorporating spherical nanoparticles in polymer matrix. The alignment of graphene and carbon nanotube sheets is a tricky process, and this problem should be eradicated even though it improves physical properties.[58] Also, mass production of defect free sheets and tubes is not feasible as it involves huge costs and time. Furthermore, graphene sheets are brittle, resulting in less flexible nanocomposites than spherical particle-based nanocomposites.[59,60] The spherical surfaces are easier to slip than sheets and tubes, which may affect the real-time monitoring capability. Therefore, spherical nanoparticles should be considered for developing strain sensors.[61,62] In addition, FDM 3D printing is a widely used technique in developing strain sensors that require the predevelopment of composite filaments, which can consume much time and cost.[33,63,64] Therefore, further research effort is needed to study the direct ink writing (DIW) of strain sensors for structural applications. Structural applications require more sensitive sensors having greater load-bearing capacity.

DIW/3D technology is used to develop flexible strain sensors with high degree of reliability for SHM. Ease of fabrication, flexibility in the design morphologies of sensors, and a large number
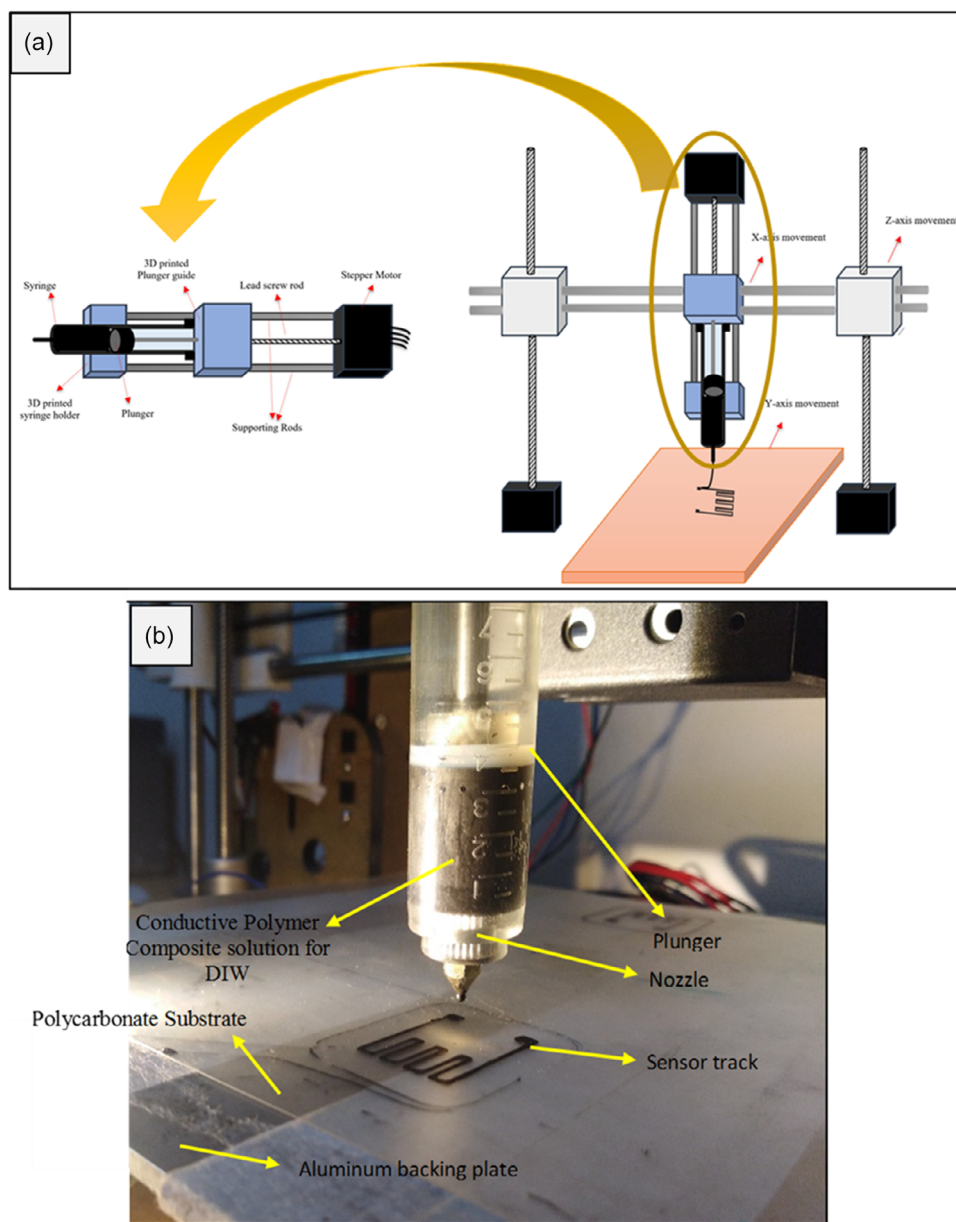


**Figure 3.** a) A schematic of syringe pump and 3D printer setup. b) DIW nozzle together with its plunger during printing operation.

of potential substrates are some of the advantages offered by DIW/3D printing. A comparison of DIW/3D printing technique employed in present work for the deposition of sensors with various other sensor fabrication techniques such as extrusion, electrospinning, spin coating, FDM, digital light processing (DLP), etc. is presented in **Figure 1**. It is evident that DIW has been used to fabricate sensors with relatively higher gauge factors (GF) as compared to other 3D printing techniques. This research presents fabrication and optimization of a novel strain gauge as a substitute for traditional metal foil strain gauges. In comparison, a polymer strain sensor blended with spherical carbon nanoparticles (CNPs), nanotubes, or graphene nanoplatelets offers greater sensitivity, flexibility, and load-bearing capacity. The sensor manufactured during this research would find its applications in overcoming problems faced by the aerospace industry such as wing flutter, mechanical vibrations, and aeroelastic tailoring.[65,66]

## 2. Experimental Section

### 2.1. Materials

Carbon nanoparticles (Printex L6) and TPU granules were provided by Orion Engineering Carbon, Germany, and Sigma Aldrich, USA, N,N-Dimethyl Formamide (DMF, 99.5%), respectively. Chloroform was purchased from Sigma Aldrich, USA. The Printex L6 was used as a conductive reinforcement in TPU. The particle size of CNP was 70 nm while the electrical conductivity was 4 S cm$^{-1}$. All the chemicals were used as received without any further treatment.

### 2.2. Conductive Polymer Composite Solution

For the development of strain gauge, a conductive polymer composite (CPC) solution comprising carbon nanoparticles (CNPs) and TPU was used. In order to prepare the solution, 50%w v$^{-1}$ TPU was dissolved in dimethyl formamide (DMF) in a beaker under magnetic stirring at 80 °C. CNPs were dispersed in DMF using ultrasonication at 20 kHz frequency. After getting the exact solution, dissolved TPU and dispersed CNPs were added together in a single beaker followed by vigorous shear mixing for 5 h at 1000 rpm and 60 °C to get CPC solution. The mixing speed was then reduced to 600 rpm. At this stage the temperature of the solution was raised by 10 °C in order to evaporate 10 mL of the solvent to achieve the viscosity required for effective 3D printing. A schematic of this process is shown in **Figure 2**.

### 2.3. Rheological Analysis of the Conductive Ink

The rheological properties of the conductive ink were determined using Brookfield DV3 rheometer. The printability of the conductive ink was characterized by varying shear rate (up to 55 s$^{-1}$) of the solution using LV-64 spindle. The effects of viscosity and shear stress were examined by plotting viscosity test and yield test. The solution–particle interaction gives a brief overview of how the materials behave under varying shear rate.

### 2.4. Fabrication of Strain Gauges: DIW/3D Printing

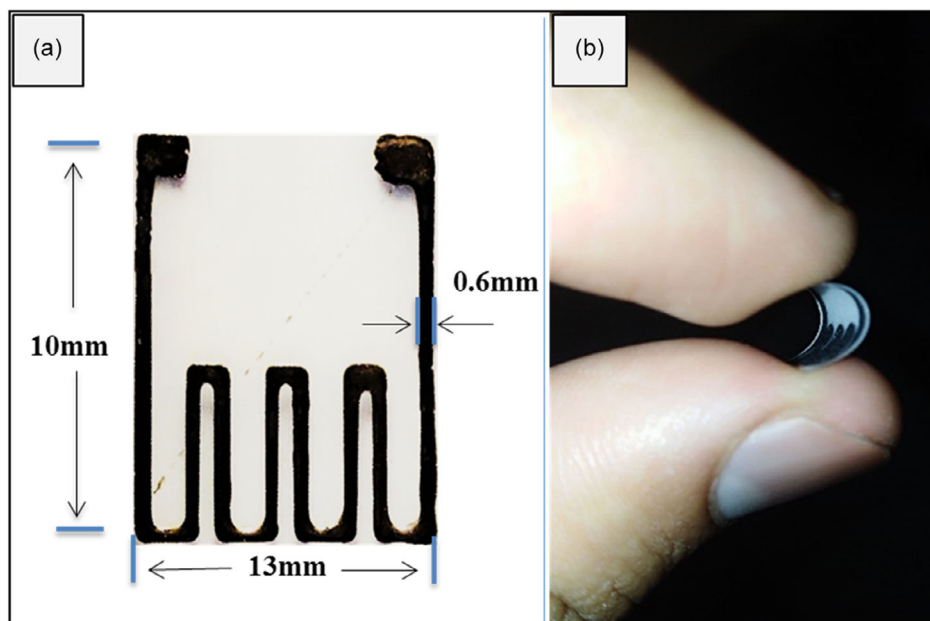The fabrication of strain gauges was carried out using a modified commercially available FDM 3D printer, Anet



**Figure 4.** a) The viscosity curve reveals shear thinning. b) The yielding threshold can be clearly distinguished by the flow capability of the ink. c) At equilibrium particles are suspended in the solution while d) at optimum shear rate, the solution shows shear thinning effect and flow characteristics. e) Layer fidelity can be seen by in situ DIW. f) Institute of Space Technology and Nottingham Trent University collaboration badge was printed by direct extrusion. g) The printed sensor shows good conductivity.
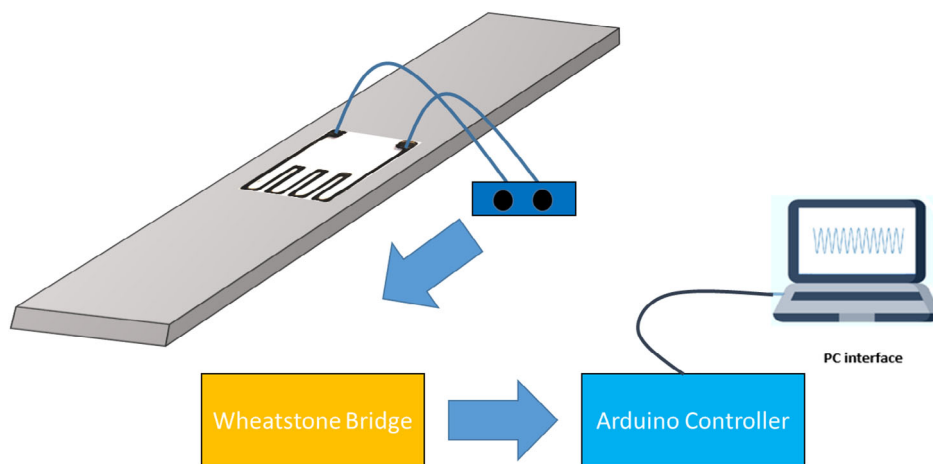
**ADVANCED
SCIENCE NEWS**

www.advancedsciencenews.com

*ADVANCED
ENGINEERING
MATERIALS*

www.aem-journal.com

**Figure 5.** a) Top view of 3D-printed strain gauge. b) Image showing flexibility and relative size of the developed strain gauge.
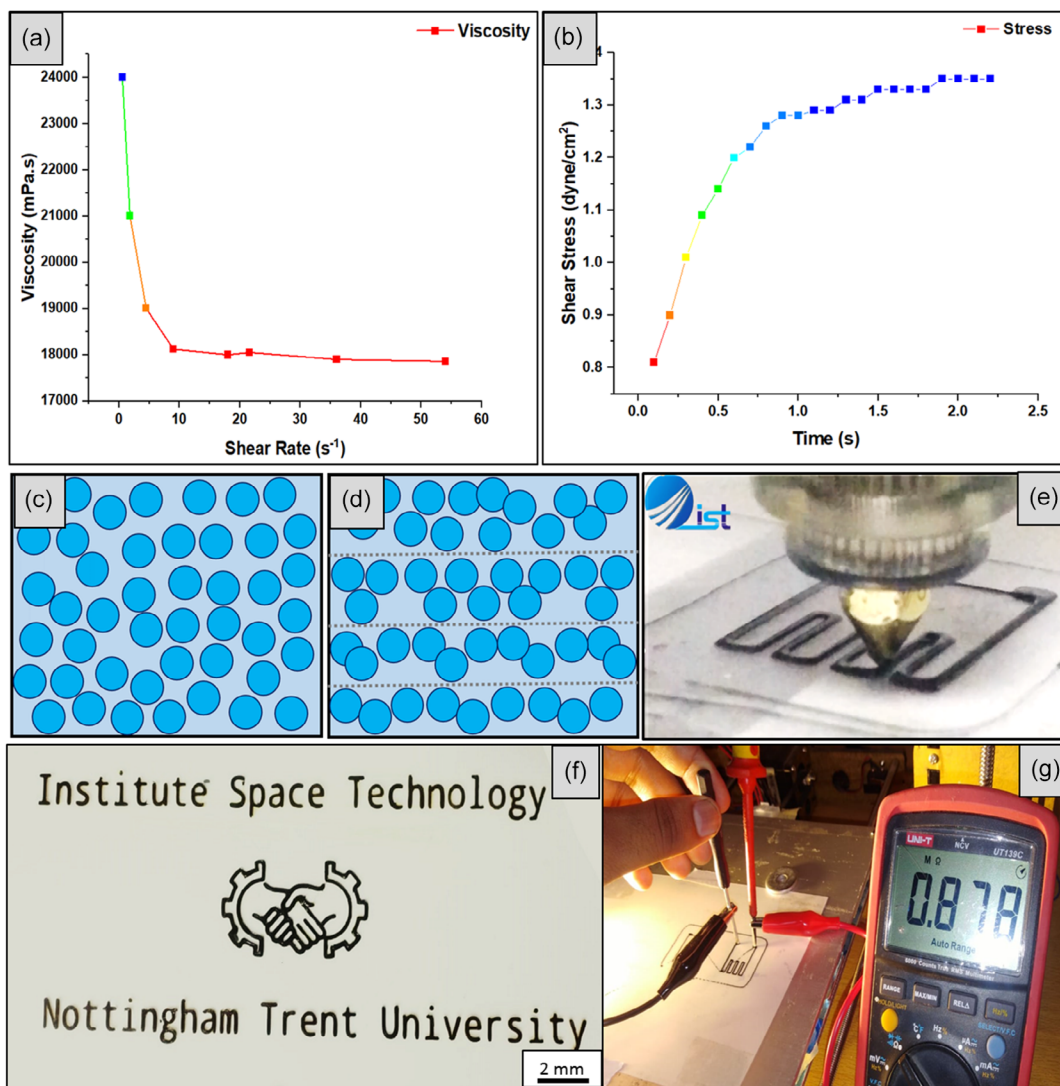


**Figure 6.** Schematic representation of the data acquisition system.

A8. First, the 3D printer was modified to incorporate DIW assembly by attaching a syringe pump nozzle in place of the extrusion nozzle to enable printing of polymer solutions and gels with greater accuracy and consistency. The DIW assembly uses a plunger to push the solution or slurry out of a fine nozzle, providing better print accuracy (**Figure 3**a).

Afterward, the CPC solution was filled in the 10 mL polycarbonate syringe prior to the execution of DIW operation. The strain gauge was printed using a 0.4 mm nozzle with bed temperature of 80 °C. The printing speed was maintained at 20 mm s$^{-1}$. The printed serpentine strain gauge pattern on a flexible TPE substrate having 122 μm thickness is shown in **Figure 4**b.

The dimensions of the printed strain gauge and its relative size are shown in **Figure 5**a,b respectively.

After printing of the strain gauge on the substrate, it was cut along specific dimensions. The strain gauge was then attached to fine copper wires using silver conductive paste provided by RS paints. These connections helped integration of the strain gauge with the data acquisition system.

## 2.5. Sensor's Response and Data Acquisition

In order to get the real-time response of the sensors on structural composites, the composite specimen was developed using Interglas 92125 plain woven glass fiber reinforcement provided by Swiss Composites (Switzerland) and two-part epoxy resin system comprising epoxy resin Araldite LY5052 and hardener Aradur 5052 provided by HUNTSMAN (USA). Eight plies of the reinforcement were laid up in order to develop cross-ply laminate [0/90/0/90]$_s$. For the calibration of strain gauge, tensile specimens were utilized according to the ASTM standard D3039 having dimensions 250 × 25 × 1.8 mm. Tabs were attached at the end of the specimens while strain gauges were pasted in the center of the specimen using epoxy resin.

The strain gauge was connected to the data acquisition system in Wheatstone bridge configuration in order to continuously determine change in its resistance during mechanical loading. For the purpose of data acquisition, Arduino microcontroller was employed to act as an analog-to-digital (ADC) converter and interface the strain gauge with a computer without the use of an additional amplifier. The acquired voltage data was then
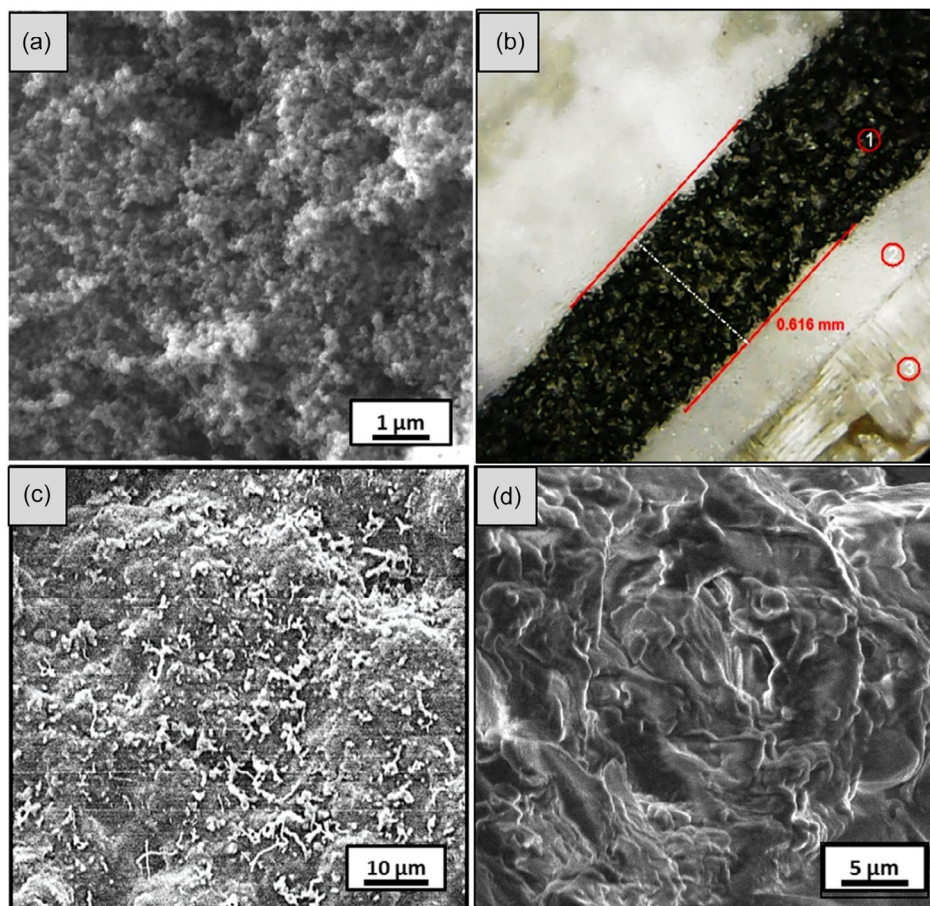


**Figure 7.** a) Morphology of the conductive CNPs. b) Image showing strain gauge attached to the composite specimen with a magnified SEM image in the inset. Three labeled regions reflect sensor track, TPE substrate, and GFRP specimen, respectively. c) Nanoparticles presence can be seen on the surface of as-fabricated strain sensor fabricated through DIW. d) The fractured surface of strain sensor.

**ADVANCED
SCIENCE NEWS**

www.advancedsciencenews.com

**ADVANCED
ENGINEERING
MATERIALS**

www.aem-journal.com

manipulated in order to determine the normalized resistance response of the strain gauge during loading. A schematic of data acquisition system is shown in **Figure 6**.

## 3. Results & Discussion

### 3.1. Rheology and Printability of the Conductive Ink

In order to get the rheological response of the conductive ink, viscosity curve and flow curve was plotted with varying shear rate. Viscosity curve reveals shear thinning effect which means increasing the shear rate results in the decrease in viscosity of the developed conductive ink[67] (Figure 4a). Flow curve reveals excellent flow and yielding characteristics of the conductive ink. Increasing the shear rate results in increasing the shear stress up to 1.2 dyne cm$^{-2}$ at which the particles starts to arrange themselves (Figure 4c,d). At 1.35 dyne cm$^{-2}$, the particles start flowing and this is the point where viscosity is overcome by increased value of shear rate and gives excellent flow characteristics of the developed ink (Figure 4b). The optimized flow characteristics result in excellent printability and layer fidelity which can be seen in Figure 4e,f. These results resembles another study.[68]

### 3.2. Morphological Analysis and the Determination of Gauge Factor

Scanning electron microscopy was used to analyze the morphology of the particles and the composite sensor deposited on the substrate. The developed DIW setup resulted in homogeneous and facile deposition of strain sensing pattern, as shown in **Figure 7**a–d.

The tensile tests were performed on glass fiber reinforced plastic (GFRP) specimens using universal testing machine (UTM) with maximum load carrying capacity of 30 kN. **Figure 8** shows the GFRP specimen with attached strain gauge loaded on UTM for tensile testing.

The developed strain gauges were pasted at the center of the specimens in order to determine the GF according to the following relationship

$$GF = \frac{dR/Ro}{\varepsilon} \qquad (1)$$

The epsilon ($\varepsilon$) is defined as change in strain divided by the original strain of the sample.

The sensitivity of the strain gauge was characterized by manufacturing the sensors at the range (0.2–1 mm) of layer width. The layer width has direct relation with the sensing structures as decreasing the layer width results in increase in the sensitivity of the sensor, as we can sense the small change in breakage of percolation network by just stretching/compressing by a small stress.[69] The result of the electromechanical characterization conducted in tensile mode is plotted in **Figure 9**. The fact that relatively high GF of 4 $\approx$ 34 was determined by linear curve fitting on normalized resistance response against strain attests to higher sensitivity of the developed strain sensor than the traditional metal foil strain gauges with reported GFs of $\approx$2. The present study was further characterized using 0.6 mm layer width. The response time and recovery time was calculated as 58 and 102 ms,



**Figure 8.** Strain gauge attached to the center of GFRP specimen for sensor calibration using tensile test.

respectively. These results would significantly play a role in the sensors and SHM industry as reported in other studies.[70,71]

### 3.3. Repeatability & Error Determination

Long-term repeatability of the sensor was determined by connecting the strain gauge printed on the TPE substrate with the two jaws of the custom-made linear actuator. The schematic diagram in **Figure 10** shows the main components of the linear actuator.

The strain gauge was attached to the jaws of the linear actuator using epoxy resin in order to prevent slippage. The crosshead speed was maintained at 50 mm min$^{-1}$ during cyclic loading. The strain gauge was maintained at 0 and repeatedly stretched to 5% strain for low strain data and prestretched to 4% strain and then the cyclic loading was applied by repeatedly stretching
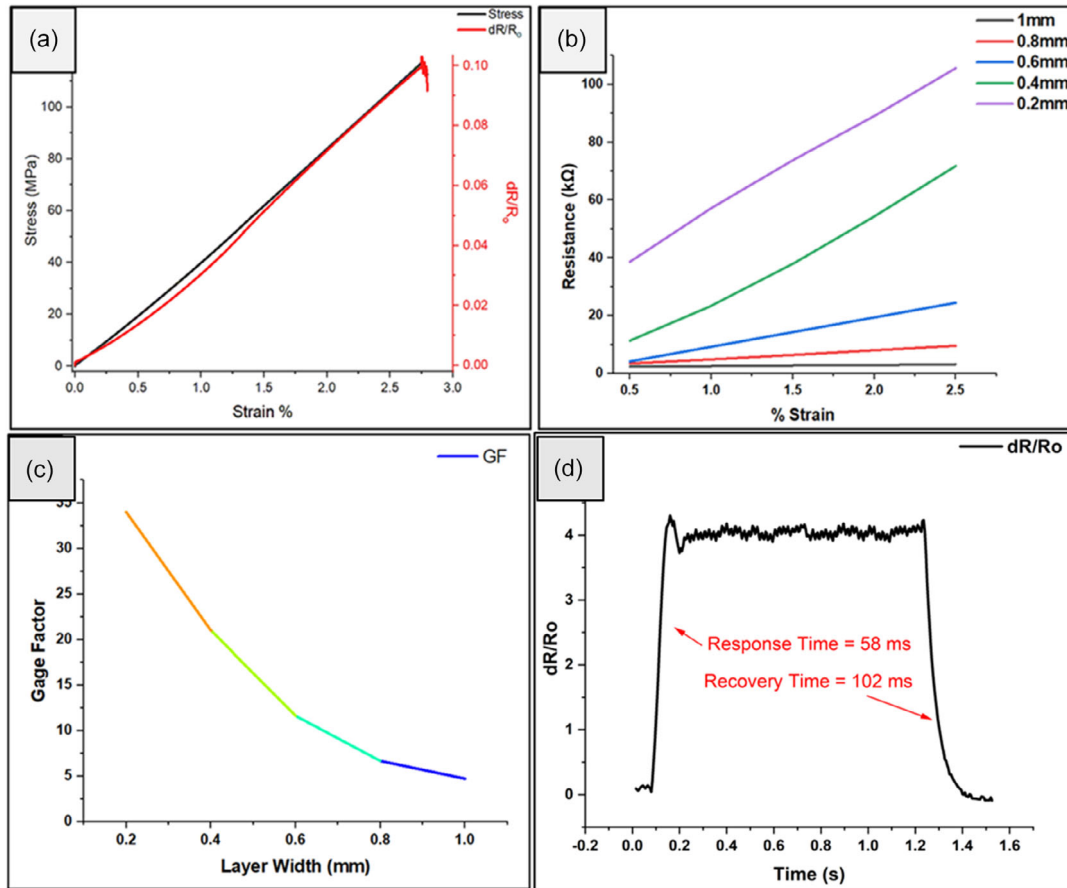
**Figure 9.** a) Normalized resistance and stress response of the GFRP specimen against strain during tensile loading. b) The resistance was plotted against the percentage strain value with varying layer width. c) The GF was compared with layer width. d) The response and recovery time of the sensor shows its effectiveness for the real systems.
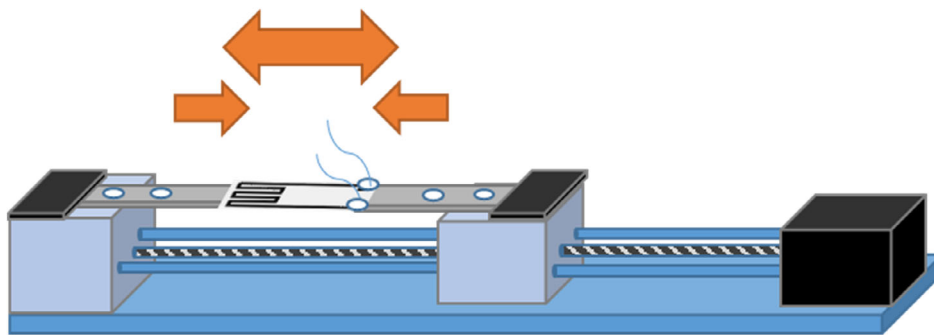


**Figure 10.** A schematic of custom-made linear actuator for cyclic testing.

the strain gauge to 10% strain for 1000 cycles. The strain gauge exhibited remarkable repeatability during the cyclic loading test, as shown in **Figure 11**.[72]

For calculation of hysteresis and integrated nonlinearity errors, normalized resistance response of three cycles was extracted to be used as sample data set, as shown in **Figure 12**. The calculated values of hysteresis and integrated nonlinearity errors were 0.034 and 0.0057, respectively.

### 3.4. Determination of *I–V* Characteristics of the Developed Strain Gauge

In order to determine the *I–V* characteristics of the developed strain gauge, it was attached to the GFRP cantilever beam, a schematic of which is shown in **Figure 13**.

The *I–V* plots are given in **Figure 14**. As shown, the input voltage was varied from 1 to 5 V while the current flowing

**ADVANCED
SCIENCE NEWS**

www.advancedsciencenews.com

**ADVANCED
ENGINEERING
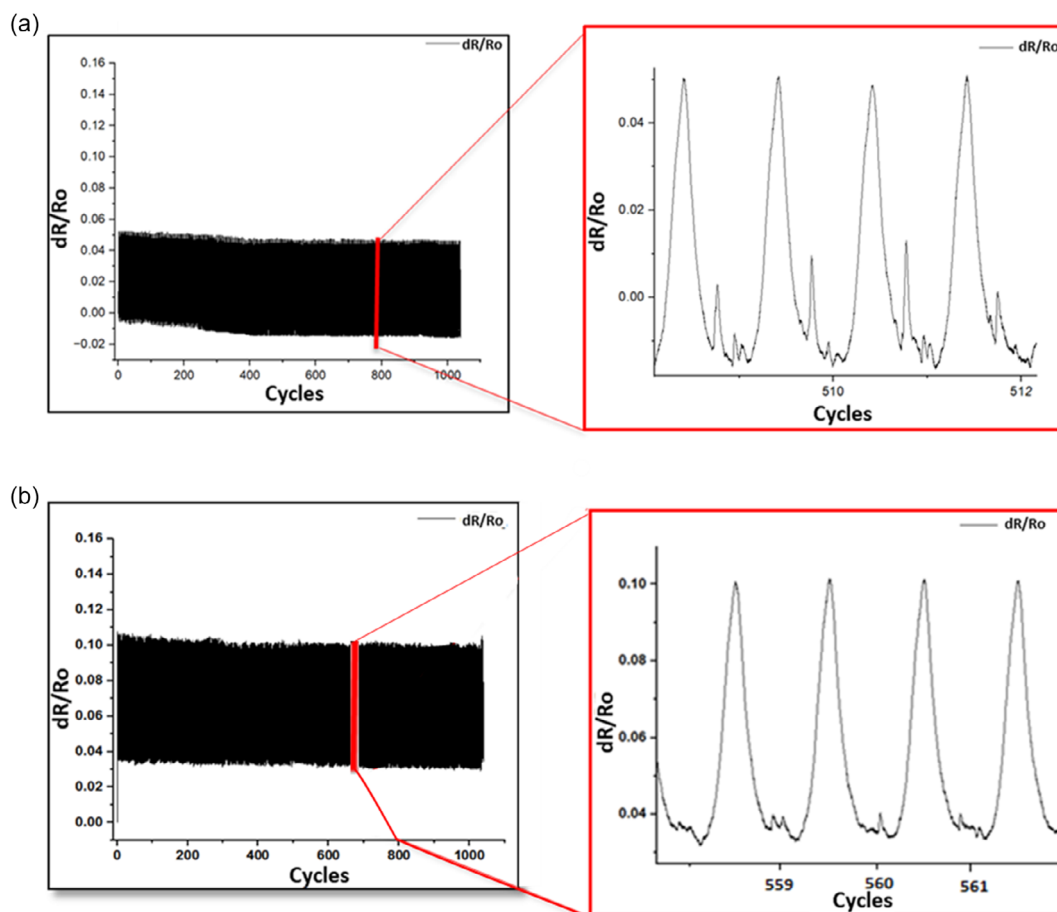MATERIALS**

www.aem-journal.com

**Figure 11.** Normalized resistance response plotted against number of cycles for the strain gauge at a) 0%–5% strain and b) 5%–10% strain.

through the strain gauge was noted. The *I–V* relationships were determined by increasing the load progressively from 0 to 5 N. A linear correspondence between the voltage and current was observed, with the plots diverting from each other at higher loads albeit exhibiting linear response in all the load ranges.[73,74]
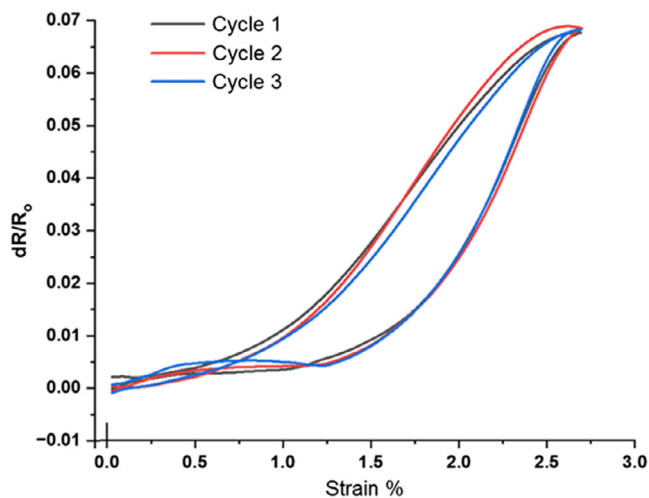
### 3.5. Thermal Behavior of Nanocomposite

Thermogravimetric (TGA) analysis of the CPC, used for the development of strain gauge, was carried out at a constant heating rate of $5\,°C\,min^{-1}$ in an inert atmosphere. The TGA plot shows 10% mass loss at 347 °C and 40% mass loss at 458 °C, due to the polymer degradation. The initial mass loss prior to complete degradation of the polymer sample can be attributed to the thermal degradation of urethane bonds.[75] This is followed by complete degradation of the polymer at 599 °C with 10% residual mass content (**Figure 15**a). We were able to get the response of the resistance with the increase in environmental temperature and we found that the developed flexible sensor is thermally stable up to 200 °C and the environment temperature has very limited influence (0.08%) on its smooth operation. It can therefore be deduced from TGA curve that CPC used for the fabrication of the sensor allows its safe operability at temperature ranges < 200 °C.



**Figure 12.** Strain hysteresis behavior of the developed sensor.

**2300763 (9 of 15)**

**ADVANCED
SCIENCE NEWS**

www.advancedsciencenews.com
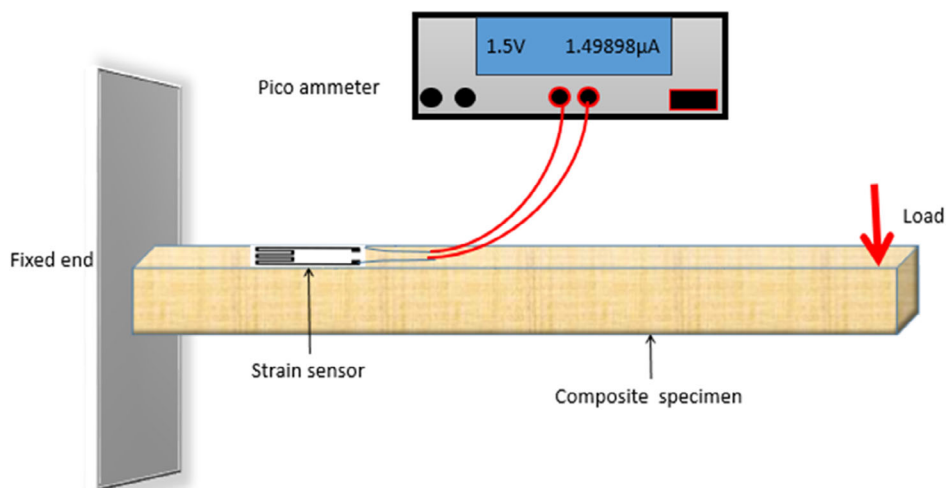
**ADVANCED
ENGINEERING
MATERIALS**

www.aem-journal.com

**Figure 13.** A schematic description of strain gauge attached to the cantilever beam for the determination of *I–V* characteristics.
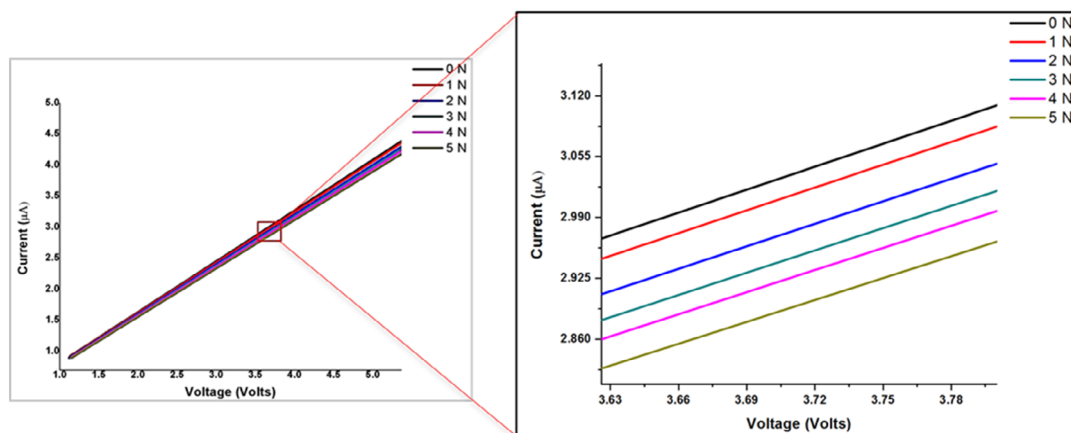


**Figure 14.** *I–V* characteristics of the developed strain gauge.
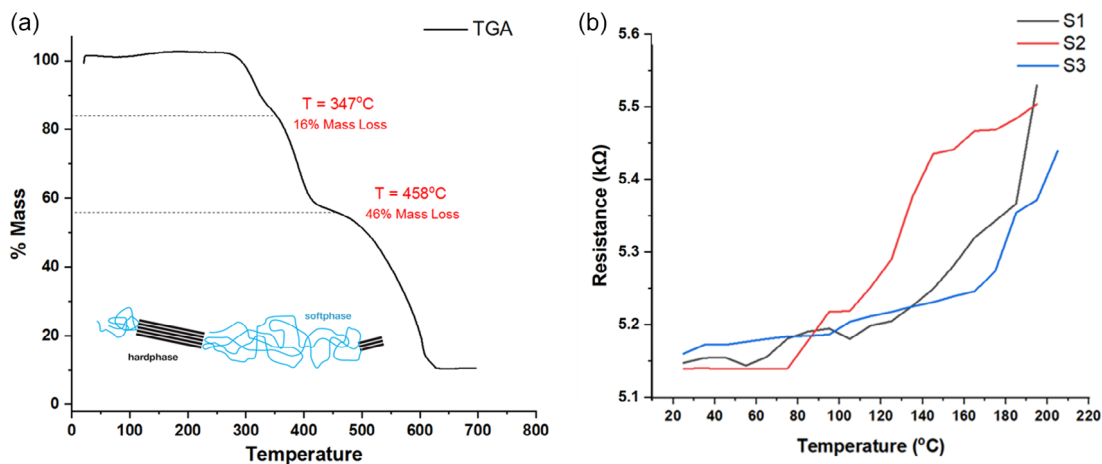


**Figure 15.** a) TGA analysis of the CPC. b) The temperature resistance behavior of sensor.
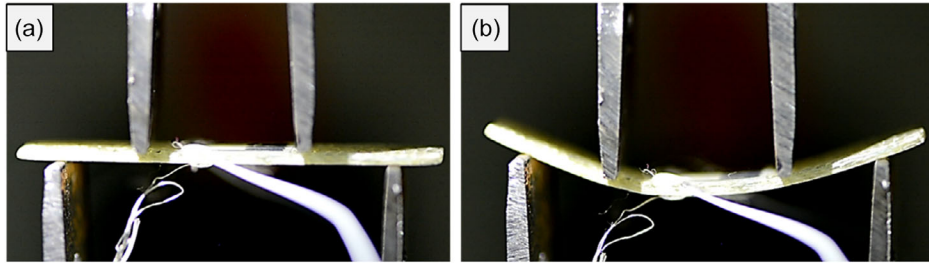
**Figure 16.** Fixture of four-point bend test: a) at the start and b) before fracture.
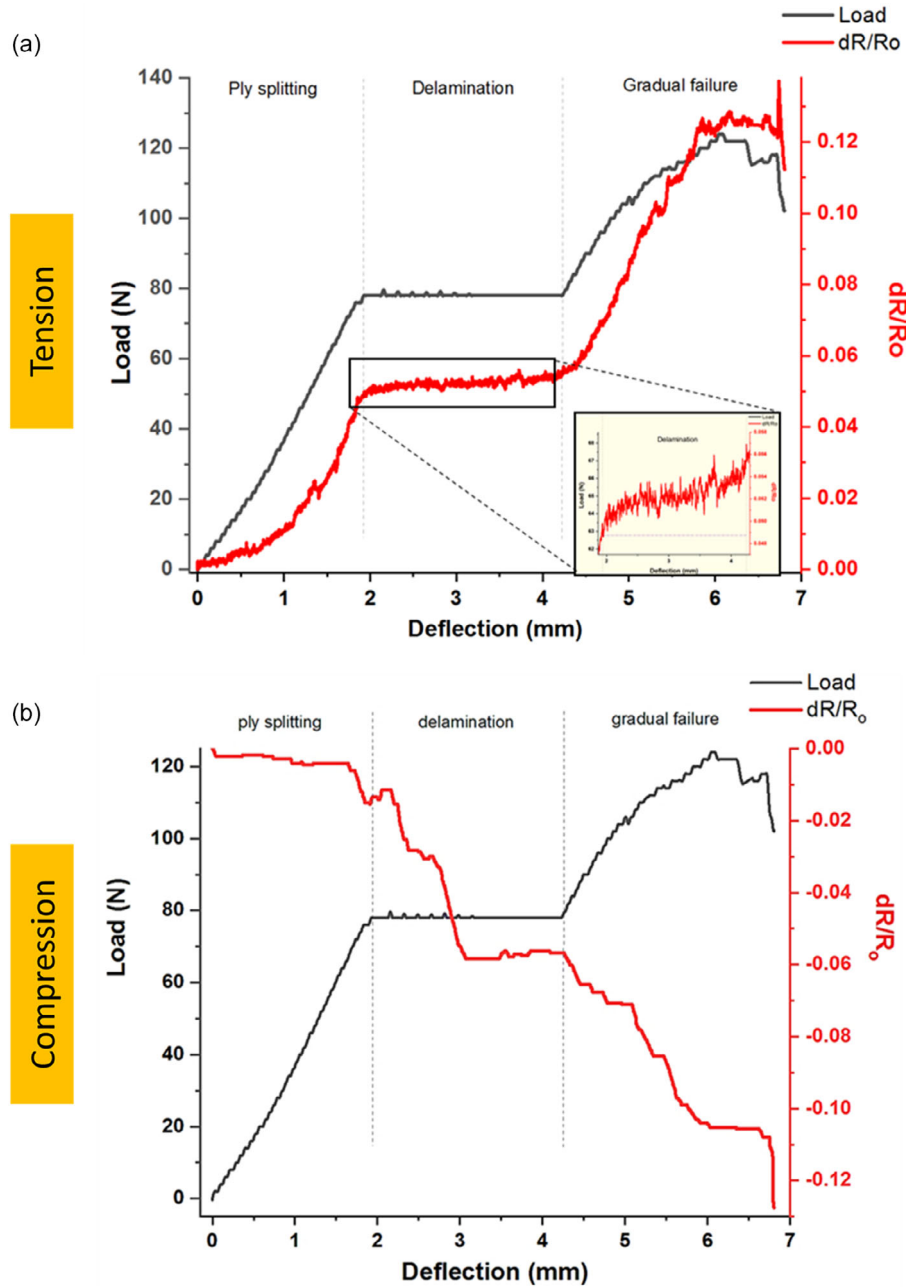


**Figure 17.** Behavior of GFRP specimen under flexural loading is compared with normalized resistance response of the strain gauge a) under tension (lower surface) and b) under compression (upper surface).

**ADVANCED
SCIENCE NEWS**

www.advancedsciencenews.com

**ADVANCED
ENGINEERING
MATERIALS**

www.aem-journal.com

### 3.6. Four-Point Flexural Tests

The developed strain gauges were attached to the four-point bending test specimens on both the faces so as to register compression and tension on the top and bottom faces respectively. To determine the flexural strength, the support span-to-thickness ratio was adjusted in such a way that the failure occurs at the outer surface of the specimens (**Figure 16**a,b). The specimen thickness was maintained at 1.8 mm, and the specimen width of 13 mm was used, with the specimen length being about 20% longer than the support span.[76] The crosshead speed was maintained at 2 mm min$^{-1}$ during the tests. The normalized resistance response of the strain gauge corresponds well with the load deflection behavior of the specimen and is able to
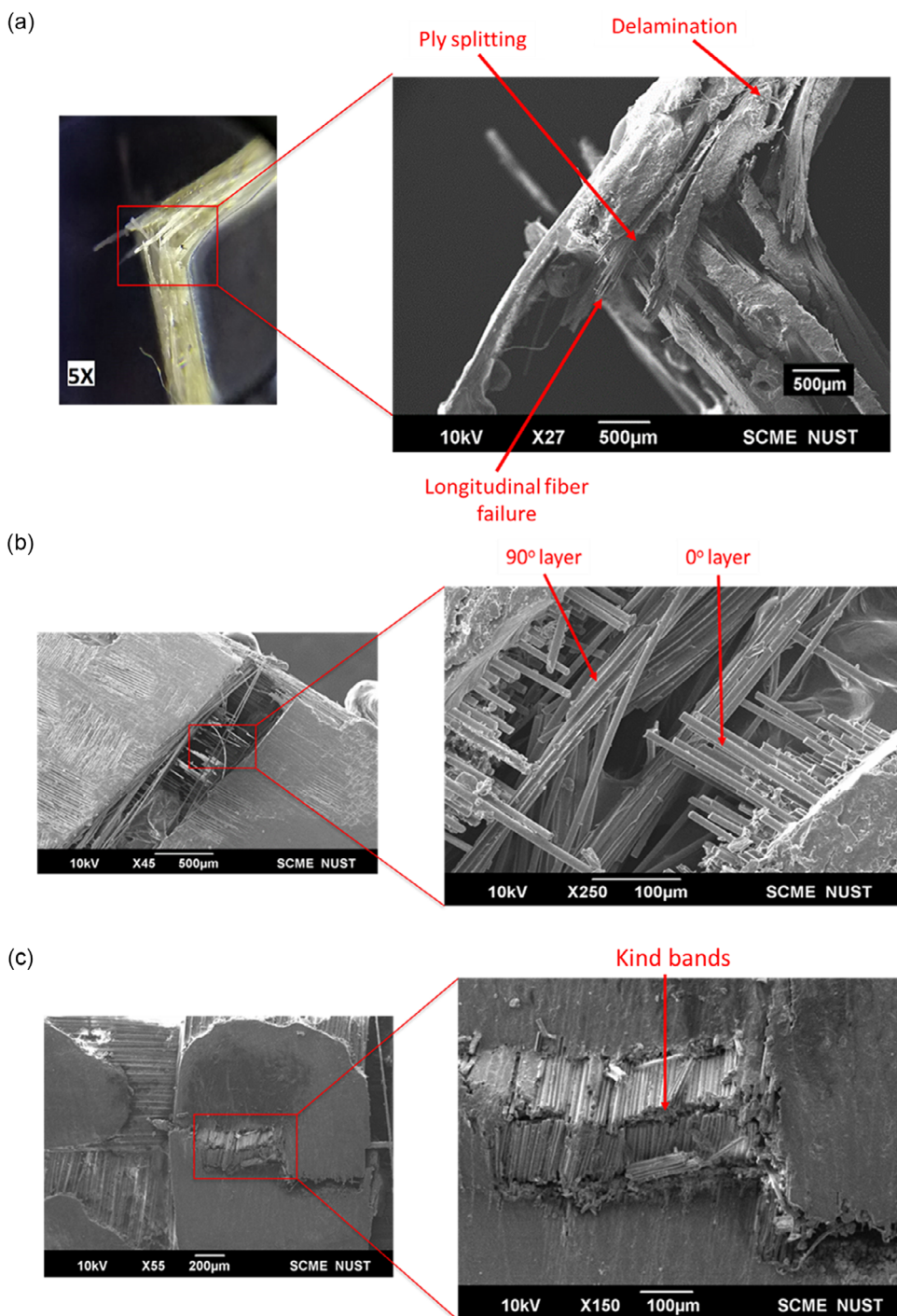


**Figure 18.** Photomicrographs showing a) side view of the fractured specimen, b) ply plitting and longitudinal fiber failure in bottom ply which failed in tension, and c) kink band formation in the top ply which failed in compression.

capture various regions in the mechanical response of the specimen, as shown in Figure 16a,b).

As expected, the general trend of the sensor response in tension points to a rise in electrical resistance due to breakage of percolation networks as embedded conductive nanoparticles keep on moving apart under tension. In both the tension and compression plots, the initial region, where electrical resistance changes rapidly, corresponds to the intralaminar failure in GFRP specimens (matrix cracking and ply splitting). This is followed by delamination region where electrical resistance changes at a slower rate (inset in **Figure 17**a) while the load remains constant as the top supports keep on moving to accentuate delamination.[77,78] In the final region where load starts increasing again, it is transferred onto the fibers, and they start failing in progressive fashion. This is evident by a gradual rise in load until the complete failure of the composite specimen. The strain gauge response in this region is that of gradual resistance change with a general increasing trend in tension and a decreasing trend in compression[79,80]

### 3.7. Fractographic Analysis

Various fractographic features could be observed on the composite specimens after flexural testing which give a clue as to the failure initiation, its progression, and specimen fracture as shown in **Figure 18**a–c. The photomicrographs showing the side view of the failed composite specimen show various failure events at the bottom face experiencing tension (Figure 18a). Under tensile loading, matrix cracking can be conjectured to have initiated the failure leading to ply splitting. The intralaminar failure modes propagate to initiate delamination as the composite specimen experiences shear due to flexural loading. The increasing load ultimately results in longitudinal fiber failure, evidence of which can also be observed at the tension face (Figure 18a,b).

The top face undergoing compression also exhibited some evidence of kink band formation, as shown in Figure 18c. It is seen that the initiation of delamination as described above would have resulted in diminution of transverse support on the top end layer. The matrix stiffness in the transverse direction as well as its shear strength also plays a role in determining the extent of microbuckling. The loss of support on the longitudinal fibers due to matrix shearing and delamination of neighboring plies resulted in the microbuckling in load bearing fibers under compression which eventually led to kink band formation.[81,82]

## 4. Conclusion

A commercial 3D printer has been modified in this research work to enable deposition of sensing patterns on various substrates using DIW attachment. A low-cost CPC solution was developed and deposited in a serpentine pattern via DIW technique on TPE substrate to manufacture high-fidelity strain gauges. The strain gauges were pasted on GFRP specimens to demonstrate their strain and damage monitoring capability. Under tensile loading, the GF achieved for the strain gauges was found to be 17 times greater than traditional metal foil strain gauges. The cyclic loading also demonstrated high repeatability

of the sensor at low (0%–5%) and high strain (4%≈10%) for 1000 cycles with low hysteresis and nonlinearity. The strain mapping and damage monitoring capability of the strain gauges was also tested by attaching these to a GFRP specimen undergoing flexural loading. The strain gauges on the two faces not only followed the general deflection pattern of the specimen in tension and compression but also registered various failure events due to their high sensitivity and flexibility. The failure behavior was correlated with the fractographic analysis which showed that the various modes of failure in the GFRP specimens did indeed lead to its fracture and the response of the developed strain gauge helped in capturing these failure events with high degree of reliability. It is therefore evident that the low-cost strain gauges developed via DIW/3D printing in this study can be used for online in situ SHM of composites. Another promising feature of this technique is its ability to deposit customized sensing patterns on various structures for their continual monitoring. Random vibration test could also be carried out on the strain sensor in the future to validate reliability specially for aerospace applications.

## Conflict of Interest

The authors declare no conflict of interest.

## Data Availability Statement

The data that support the findings of this study are available from the corresponding author upon reasonable request.

[1] F. J. Pallarés, M. Betti, G. Bartoli, L. Pallarés, *Constr. Build. Mater* **2021**, *297*, 123768.

[2] H. Momeni, A. Ebrahimkhanlou, *Smart Mater. Struct.* **2022**, *31*, 43001.

[3] A. Tiwary, R. Kumar, J. S. Chohan, *Mater. Today Proc.* **2022**, *51*, 865.

[4] W. Zhao, H. Chen, Y. Zhang, D. Zhou, L. Liang, B. Liu, T. Xu, *Bioeng. Transl. Med.* **2022**, *7*, e10303.

[5] I. Sioutis, K. Tserpes, *Aerospace* **2023**, *10*, 137.

[6] C. Wu, F. Lin, X. Pan, Z. Cui, Y. He, G. Chen, X. Liu, G. He, Q. Chen, D. Sun, Z. Hai, *Adv. Eng. Mater.* **2022**, *24*, 2200228.

[7] V. Giurgiutiu, in *Polymer Composites In The Aerospace Industry (Second Edition)*, (Eds: P. Irving, C. Soutis), 2nd ed., Woodhead Publishing

2020, pp. 491–558, https://doi.org/10.1016/B978-0-08-102679-3.00017-4.

[8] A. M. Abdel-Latif, in *Damage and Fracture Mechanics*, (Eds: T. Boukharouba, M. Elboujdaini, G. Pluvinage), Springer Netherlands, Dordrecht 2009, pp. 93–100.

[9] J. Diaz-Escobar, P. Díaz-Montiel, S. Venkataraman, A. Díaz-Ramírez, *Struct. Control Health Monit.* 2023, 2023, 1675867.

[10] F. Ciampa, P. Mahmoodi, F. Pinto, M. Meo, *Sensors* 2018, 18, 609.

[11] H. Zhang, T. Liu, J. Lu, R. Lin, C. Chen, Z. He, S. Cui, Z. Liu, X. Wang, B. Liu, K. Xiong, Q. Wu, *Opt. Fiber Technol.* 2023, 78, 103316.

[12] S. Nauman, Z. Asfar, S. Ahmed, M. A. Nasir, N. A. Hocine, *J. Thermoplast. Compos. Mater.* 2023, 36, 234.

[13] M. Anas, M. A. Nasir, Z. Asfar, S. Nauman, M. Akalın, F. Ahmad, *J. Braz. Soc. Mech. Sci. Eng.* 2018, 40, 1.

[14] R. Jan, A. Habib, Z. M. Khan, M. B. Khan, M. Anas, A. Nasir, S. Nauman, *J. Intell. Mater. Syst. Struct.* 2017, 28, 1565.

[15] M. A. Nasir, H. Akram, Z. M. Khan, M. Shah, S. Anas, Z. Asfar, S. Nauman, *J. Intell. Mater. Syst. Struct.* 2015, 26, 2362.

[16] S. Ahmed, S. Nauman, Z. M. Khan, in *2021 Inter. Bhurban Conf. on Applied Sciences and Technologies (IBCAST)*, IEEE, Islamabad, Pakistan 2021, pp. 47–54.

[17] D. M. McCann, M. C. Forde, *NDT & E Int.* 2001, 34, 71.

[18] J. Park, K. Shin, C. Lee, *Int. J. Precis. Eng. Manuf.* 2016, 17, 537.

[19] W. J. Staszewski, C. Boller, S. Grondel, C. Biemans, E. O'Brien, C. Delebarre, G. R. Tomlinson, in *Health Monitoring of Aerospace Structures*, John Wiley & Sons, Ltd 2003, pp. 125–162, https://doi.org/10.1002/0470092866.ch4.

[20] V. Giurgiutiu, J. M. Redmond, D. P. Roach, K. Rackow, in *Smart Structures and Materials 2000: Smart Structures and Integrated Systems*, (Ed: N. M. Wereley), Society of Photo-Optical Instrumentation Engineers (SPIE) Conf. Series, Vol. 3985, June 2000, pp. 294–305, https://doi.org/10.1117/12.388833.

[21] S. Nauman, I. Cristian, V. Koncar, *Text. Res. J.* 2012, 82, 931.

[22] S. Nauman, I. Cristian, V. Koncar, *Sensors* 2011, 11, 9478.

[23] K. Ono, *Appl. Sci.* 2019, 9, 1575.

[24] D. Kinet, P. Mégret, K. W. Goossen, L. Qiu, D. Heider, C. Caucheteur, *Sensors* 2014, 14, 7394.

[25] Glowing under strain - Aerospace America, https://aerospaceamerica.aiaa.org/departments/glowing-under-strain/.

[26] A. Mahmud, A. A. Khan, P. Voss, T. Das, E. Abdel-Rahman, D. Ban, *Adv. Mater. Interfaces* 2018, 5, 1801167.

[27] J. dosReis, C. Oliveira Costa, J. da Costa, *Struct. Control Health Monit.* 2018, 25, e2264.

[28] Y. Khan, A. Thielens, S. Muin, J. Ting, C. Baumbauer, A. C. Arias, *Adv. Mater.* 2020, 32, 1905279.

[29] Y. Zheng, Y. Li, Z. Li, Y. Wang, K. Dai, G. Zheng, C. Liu, C. Shen, *Compos. Sci. Technol.* 2017, 139, 64.

[30] T. Yan, Z. Wang, Z. Pan, *Curr. Opin. Solid State Mater. Sci.* 2018, 22, 213.

[31] J. Tang, Y. Wu, S. Ma, T. Yan, Z. Pan, *Composites, Part B Eng.* 2022, 232, 109605.

[32] Y. Fang, J. Xu, F. Gao, X. Du, Z. Du, X. Cheng, H. Wang, *Composites, Part B Eng.* 2021, 219, 108965.

[33] H. Nassar, R. Dahiya, in *2022 IEEE Inter. Conf. on Flexible and Printable Sensors and Systems (FLEPS)*, IEEE, Vienna, Austria 2022, pp. 1–4.

[34] M. A. Saleh, R. Kempers, G. W. Melenka, *Smart Mater. Struct.* 2019, 28, 105041.

[35] F. Yin, D. Ye, C. Zhu, L. Qiu, Y. Huang, *Sensors* 2017, 17, 2677.

[36] Y. Wang, Y. Jia, Y. Zhou, Y. Wang, G. Zheng, K. Dai, C. Liu, C. Shen, *J. Mater. Chem. C* 2018, 6, 8160.

[37] J. F. Christ, N. Aliheidari, P. Pötschke, A. Ameli, *Polymers* 2019, 11, 11.

[38] K. Yang, F. Yin, D. Xia, H. Peng, J. Yang, W. Yuan, *Nanoscale* 2019, 11, 9949.

[39] J. Lee, S. Shin, S. Lee, J. Song, S. Kang, H. Han, S. Kim, S. Kim, J. Seo, D. Kim, T. Lee, *ACS Nano* 2018, 12, 4259.

[40] M. Wajahat, S. Lee, J. H. Kim, W. S. Chang, J. Pyo, S. H. Cho, S. K. Seol, *ACS Appl. Mater. Interfaces* 2018, 10, 19999.

[41] Y. Chen, Y. Zhang, F. Song, H. Zhang, Q. Zhang, J. Xu, H. Wang, F. Ke, *Adv. Mater. Technol.* 2021, 6, 2100421.

[42] Y. Yao, B. Glisic, *Sensors* 2015, 15, 8088.

[43] J. Lee, S. Kim, J. Lee, D. Yang, B. C. Park, S. Ryu, I. Park, *Nanoscale* 2014, 6, 11932.

[44] P. Zhang, Y. Chen, Y. Li, Y. Zhang, J. Zhang, L. Huang, *Sensors* 2020, 20, 1154.

[45] H. Li, J. Chen, X. Chang, Y. Xu, G. Zhao, Y. Zhu, Y. Li, *J. Mater. Chem. A* 2021, 9, 1795.

[46] M. Amjadi, A. Pichitpajongkit, S. Lee, S. Ryu, I. Park, *ACS Nano* 2014, 8, 5154.

[47] D. Xiang, X. Zhang, Y. Li, E. Harkin-Jones, Y. Zheng, L. Wang, C. Zhao, P. Wang, *Composites, Part B Eng.* 2019, 176, 107250.

[48] H.-G. Kim, S. Hajra, D. Oh, N. Kim, H. J. Kim, *Composites, Part B Eng.* 2021, 222, 109079.

[49] B. Li, S. Zhang, L. Zhang, Y. Gao, F. Xuan, *J. Manuf. Processes* 2022, 74, 283.

[50] D. G. Bekas, Y. Hou, Y. Liu, A. Panesar, *Composites, Part B Eng.* 2019, 179, 107540.

[51] X. Wang, M. Jiang, Z. Zhou, J. Gou, D. Hui, *Composites, Part B Eng.* 2017, 110, 442.

[52] D. Xiang, X. Zhang, E. Harkin-Jones, W. Zhu, Z. Zhou, Y. Shen, Y. Li, C. Zhao, P. Wang, *Composites, Part A Appl. Sci. Manuf.* 2020, 129, 105730.

[53] W. Gul, S. R. Akbar Shah, A. Khan, N. Ahmad, S. Ahmed, N. Ain, A. Mehmood, B. Salah, S. S. Ullah, R. Khan, *Front. Mater.* 2023, 10, 1206918.

[54] S. Ahmed, S. Nauman, Z. M. Khan, *J. Thermoplast. Compos. Mater.* 2023, 36, 2459.

[55] S.-W. Dai, Y.-L. Gu, L. Zhao, W. Zhang, C.-H. Gao, Y.-X. Wu, S.-C. Shen, C. Zhang, T.-T. Kong, Y.-T. Li, L.-X. Gong, G.-D. Zhang, L.-C. Tang, *Composites, Part B Eng.* 2021, 225, 109243.

[56] J. Hwang, Y. Kim, H. Yang, J. H. Oh, *Composites, Part B Eng.* 2021, 211, 108607.

[57] J. Yin, C. Lu, C. Li, Z. Yu, C. Shen, Y. Yang, X. Jiang, Y. Zhang, *Composites, Part B Eng.* 2022, 230, 109528.

[58] F. Wang, H. Wang, J. Mao, *J. Mater. Sci.* 2019, 54, 36.

[59] W. S. AbuShanab, E. B. Moustafa, E. Ghandourah, M. A. Taha, *Results Phys.* 2020, 19, 103343.

[60] D. G. Papageorgiou, I. A. Kinloch, R. J. Young, *Prog. Mater. Sci.* 2017, 90, 75.

[61] J. C. Martinez-Garcia, A. Serraïma-Ferrer, A. Lopeandía-Fernández, M. Lattuada, J. Sapkota, J. Rodríguez-Viejo, *Nanomater.* 2021, 11, 830.

[62] A. Karatrantos, N. Clarke, R. J. Composto, K. I. Winey, *Soft Matter* 2016, 12, 2567.

[63] J. F. Christ, in *3D Printing of Strain Sensors*, Washington State University, Pullman, Washington 2017.

[64] M. Alsharari, B. Chen, W. Shu, *Proceedings* 2018, 2, 792.

[65] F. Boussu, B. Provost, M. Lefebvre, D. Coutellier, *Adv. Mater. Sci. Eng.* 2019, 2019, 7938720.

[66] (Ed: S. Vassiliadis), in *Advances in Modern Woven Fabrics Technology*, IntechOpen, Rijeka 2011.

2300763 (14 of 15)

[67] P. A. Amorim, M. A. d'Ávila, R. Anand, P. Moldenaers, P. Van Puyvelde, V. Bloemen, *Bioprinting* **2021**, *22*, e00129.

[68] L. Jiang, Y. C. Lam, K. C. Tam, D. T. Li, J. Zhang, *Polym. Bull.* **2006**, *57*, 575.

[69] S. Shin, B. Ko, H. So, *Microsyst. Nanoeng.* **2022**, *8*, 12.

[70] N. Munasinghe, M. Woods, L. Miles, G. Paul, in *2019 IEEE Inter. Conf. on Cybernetics and Intelligent Systems (CIS) and IEEE Conf. on Robotics, Automation and Mechatronics (RAM)*, IEEE, Bangkok, Thailand **2019**, pp. 275–280.

[71] M. Liu, Q. Zhang, Y. Shao, C. Liu, Y. Zhao, *Micromachines* **2019**, *10*, 20.

[72] H. Liu, H. Zhang, W. Han, H. Lin, R. Li, J. Zhu, W. Huang, *Adv. Mater.* **2021**, *33*, 2004782.

[73] S. Han, C. Liu, H. Xu, D. Yao, K. Yan, H. Zheng, H.-J. Chen, X. Gui, S. Chu, C. Liu, *Npj Flexible Electron.* **2018**, *2*, 16.

[74] Y.-G. Kim, J.-H. Song, S. Hong, S.-H. Ahn, *Npj Flexible Electron.* **2022**, *6*, 52.

[75] M. Dong, Q. Li, H. Liu, C. Liu, E. K. Wujcik, Q. Shao, T. Ding, X. Mai, C. Shen, Z. Guo, *Polymer* **2018**, *158*, 381.

[76] Z. Raheem, *Designation: D 7264/D 7264M -07 Standard Test Method for Flexural Properties of Polymer Matrix Composite Materials* **2020**, 1.

[77] H. Ullah, A. R. Harland, V. V. Silberschmidt, *Appl. Compos. Mater.* **2012**, *19*, 769.

[78] R. A. Naik, *J. Compos. Mater.* **1995**, *29*, 2334.

[79] Y. Bai, T. Keller, C. Wu, *Mater. Struct.* **2013**, *46*, 1143.

[80] K. Gao, Z. Zhang, S. Weng, H. Zhu, H. Yu, T. Peng, *Appl. Sci.* **2022**, *12*, 9750.

[81] S. Gohari, S. Sharifi, C. Burvill, S. Mouloodi, M. Izadifar, P. Thissen, *Arch. Civ. Mech. Eng.* **2019**, *19*, 1235.

[82] Z. Omar, S. Sugiman, M. M. Yussof, H. Ahmad, *Case Stud. Constr. Mater.* **2022**, *17*, e01503.